Available online at www.sciencedirect.com
ScienceDirect
Journal of Power Sources 160 (2006) 662–673
JOURNAL OF POWER SOURCES
www.elsevier.com/locate/jpowsour

Power and thermal characterization of a lithium-ion battery pack for hybrid-electric vehicles

Kandler Smith, Chao-Yang Wang *

Electrochemical Engine Center (ECEC), Department of Mechanical and Nuclear Engineering, The Pennsylvania State University, University Park, PA 16802, USA

Received 24 October 2005; received in revised form 6 January 2006; accepted 11 January 2006
Available online 13 February 2006

Abstract

A 1D electrochemical, lumped thermal model is used to explore pulse power limitations and thermal behavior of a 6 Ah, 72 cell, 276 V nominal Li-ion hybrid-electric vehicle (HEV) battery pack. Depleted/saturated active material Li surface concentrations in the negative/positive electrodes consistently cause end of high-rate (∼25 C) pulse discharge at the 2.7 V cell^{-1} minimum limit, indicating solid-state diffusion is the limiting mechanism. The 3.9 V cell^{-1} maximum limit, meant to protect the negative electrode from lithium deposition side reaction during charge, is overly conservative for high-rate (∼15 C) pulse charges initiated from states-of-charge (SOCs) less than 100%. Two-second maximum pulse charge rate from the 50% SOC initial condition can be increased by as much as 50% without risk of lithium deposition. Controlled to minimum/maximum voltage limits, the pack meets partnership for next generation vehicles (PNGV) power assist mode pulse power goals (at operating temperatures >16 °C), but falls short of the available energy goal.

In a vehicle simulation, the pack generates heat at a 320 W rate on a US06 driving cycle at 25 °C, with more heat generated at lower temperatures. Less aggressive FUDS and HWFET cycles generate 6–12 times less heat. Contact resistance ohmic heating dominates all other mechanisms, followed by electrolyte phase ohmic heating. Reaction and electronic phase ohmic heats are negligible. A convective heat transfer coefficient of $h = 10.1$ W m^{-2} K^{-1} maintains cell temperature at or below the 52 °C PNGV operating limit under aggressive US06 driving.

Keywords: Lithium-ion battery; Electrochemical modeling; Hybrid-electric vehicles; Transient; Solid-state diffusion; Heat generation

1. Introduction

While much understanding of internal processes and limitations of Li-ion batteries has come from fundamentally based models [1–10], until recently none of those models had been extended to describe batteries designed for hybrid-electric vehicles (HEVs) [11]. The majority of the literature is instead devoted to predicting energy available and heat generated at various discharge rates beginning from the fully charged state. Although relevant to cell phone, laptop, and perhaps electric vehicle batteries, such works offer little insight into physical limitations expected under HEV operation where batteries are used as a transient pulse power source, cycled about a relatively fixed state of charge (SOC).

Pulse power requirements for HEV batteries are generally specified in terms of a characteristic time, rather than maximum C-rate. Partnership for next generation vehicles (PNGV) energy storage program goals [12] in power assist mode target a 25 kW pulse discharge power capability lasting 18 s and a 30 kW pulse charge capability lasting 2 s. Within the SOC operating range capable of meeting the power goals, a minimum of 0.3 kWh energy must be available. PNGV test procedures dictate the use of hybrid pulse power characterization (HPPC) test data to parameterize an equivalent circuit model with a polarization resistance for the characteristic pulse duration. The equivalent circuit model is then used to extrapolate those test results to define maximum 18 s discharge and 2 s charge current-rate capability. While the method is quick and practical to implement, caution should be exercised when extending any empirical model outside its region of validation. In contrast, full experimental characterization provides the best accuracy with the obvious drawback of requiring several hundred hours of testing.

* Corresponding author. Tel.: +1 814 863 4762; fax: +1 814 863 4848.
E-mail address: cxw31@psu.edu (C.-Y. Wang).

0378-7753/$ – see front matter © 2006 Elsevier B.V. All rights reserved.
doi:10.1016/j.jpowsour.2006.01.038

Nomenclature

a_s	active surface area per electrode unit volume ($cm^2\ cm^{-3}$)
A	electrode plate area (cm^2)
c	volume-averaged concentration of lithium in a phase ($mol\ cm^{-3}$)
D	diffusion coefficient of lithium species ($cm^2\ s^{-1}$)
E_{act}	activation energy ($J\ mol^{-1}$)
F	Faraday's constant, 96,487 $C\ mol^{-1}$
h	convective heat transfer coefficient ($W\ m^{-2}\ K^{-1}$)
i_0	exchange current density of an electrode reaction ($A\ cm^{-2}$)
I	applied current (A)
j	reaction current resulting in production or consumption of a species ($A\ cm^{-3}$)
l_s	diffusion length of lithium in solid phase (cm)
L	cell width (cm)
q_c	ohmic heat generation rate due to contact resistance (W)
q_j	ohmic (joule) heat generation rate of solid and electrolyte phases (W)
q_r	heat generation rate of electrochemical reaction (W)
r	radial coordinate along active material particle (cm)
R	universal gas constant, 8.3143 $J\ mol^{-1}\ K^{-1}$
R_f	film resistance on an electrode surface ($\Omega\ cm^2$)
R_s	radius of solid active material particles (cm)
t	time (s)
t_+^0	transference number of lithium ion with respect to the velocity of solvent
T	absolute temperature (K)
U	open-circuit potential of an electrode reaction (V)
x	negative electrode solid phase stoichiometry and coordinate along the cell width (cm)
y	positive electrode solid phase stoichiometry

Greek symbols

α_a, α_c	anodic and cathodic transfer coefficients for an electrode reaction
ε	volume fraction or porosity of a phase
η	surface overpotential of an electrode reaction (V)
κ	conductivity of an electrolyte ($S\ cm^{-1}$)
κ_D	diffusional conductivity of a species ($A\ cm^{-1}$)
σ	conductivity of solid active materials in an electrode ($S\ cm^{-1}$)
ϕ	volume-averaged electrical potential in a phase (V)
Ψ	generic physiochemical property

Subscripts

e	electrolyte phase
max	maximum value
ref	with respect to a reference state
s	solid phase
s,avg	average, or bulk solid phase
s,e	solid/electrolyte interface
sep	separator region
−	negative electrode region
+	positive electrode region
0%	zero state of charge (fully discharged) reference state
100%	100% state of charge (fully charged) reference state

Superscripts

eff	effective
Li	lithium species

Thermal behavior of Li-ion batteries has been of interest due to their potential for thermal runaway and explosion under high temperature operation. Researchers have approached the problem through both experiment and modeling [8,9,13–19]. Nelson et al. [19] used a lumped-parameter model to explore the ability of HEV cell designs of various geometry to meet PNGV power and thermal requirements. Coupled with a vehicle simulator, Nelson's model predicted a worst-case cooling requirement of 250 W on a modified HWFET driving cycle, with normal HWFET speeds multiplied by 1.3 to simulate aggressive, high speed driving.

Smith and Wang [11] recently extended a previously developed [8] 1D electrochemical, lumped thermal Li-ion battery model to describe a 72 cell, 276 V nominal, 6 Ah HEV battery pack. Validated against 1 C discharge and charge, HPPC, and driving cycle data sets, the model is used in this work to predict battery pack power rate capability with respect to PNGV goals over a range of SOC and operating temperatures. Unlike equivalent circuit models popular for HEV battery beginning-of-life characterization [20], aging characterization [21,22], and control-law development [23–25], the model provides physical explanation of the limits of operation. Furthermore, the battery model is integrated into a vehicle simulator to quantify and explain battery heat generation rates expected in a midsize passenger car application for a range of driving cycles and operating temperatures.

2. Mathematical model

Shown in Fig. 1, the 1D Li-ion cell model consists of three regions—the negative composite electrode (with Li_xC_6 active material), an electron-blocking separator, and positive composite electrode (with a metal oxide active material such as Li_yCoO_2). During discharge, lithium ions inside of solid Li_xC_6 particles diffuse to the surface where they react and transfer from the solid phase into the electrolyte phase. The positively charged ions travel via diffusion and migration through the electrolyte solution to the positive electrode where they react and insert into solid metal oxide particles. Electrons follow an opposite path through an external circuit or load. Here, we briefly

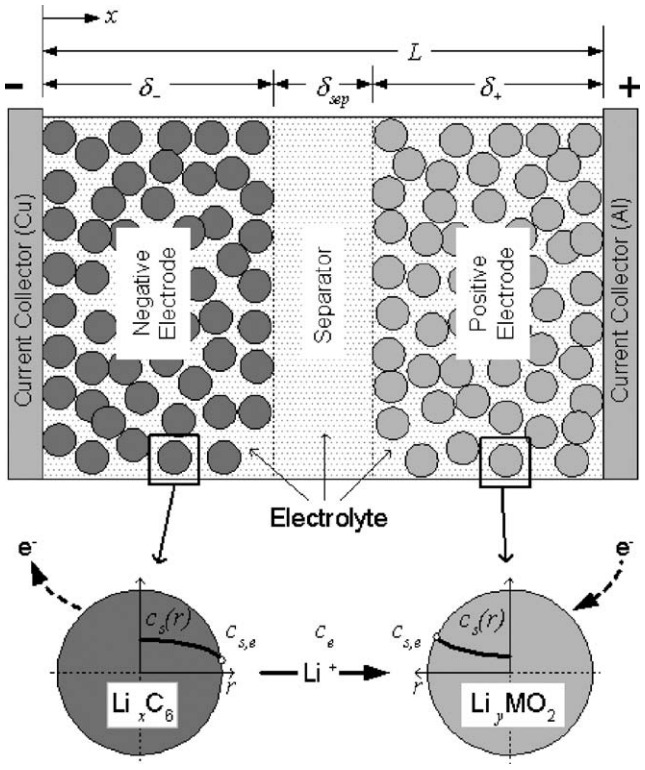

Fig. 1. Schematic of 1D (x-direction) electrochemical cell model with coupled 1D microscopic (r-direction) solid diffusion model.

summarize that 1D electrochemical model and introduce the coupled lumped thermal model.

2.1. 1D electrochemical model

The 1D domain is subdivided into electrolyte and solid phases, denoted by subscripts e and s, respectively. The electrolyte phase is continuous across the cell domain while the solid phase exists only in the negative and positive electrodes. Charge (e^-) conservation governs phase potentials, ϕ_e and ϕ_s, while Li species conservation governs phase concentrations, c_e and c_s. A Butler–Volmer kinetic equation couples charge and species governing equations by describing the volume-specific rate of reaction, j^{Li}, occurring at the solid/electrolyte interface as a function of overpotential, η. Overpotential is defined as the difference between solid and electrolyte phase potentials, minus the solid phase equilibrium potential, or $\eta = \phi_s - \phi_e - U$, where local equilibrium potential, U, is a strong function of solid phase Li concentration at the solid/electrolyte interface, $c_{s,e}$. The rate at which solid phase Li species diffuse from inner bulk regions of active material particles to the surface is the predominant limiting mechanism during high rate discharge [11,26] of the cell studied in this work. (Note that we use the terms "solid/electrolyte interface" and "solid particle surface" interchangeably.)

Cell terminal voltage is the difference in solid phase potential between the two current collectors, minus an ohmic drop due to contact resistance, or

$$V = \phi_s|_{x=L} - \phi_s|_{x=0} - \frac{R_f}{A} I. \tag{1}$$

Table 1
1D electrochemical model equations

Conservation equations		Boundary conditions
Species, electrolyte phase	$\frac{\partial(\varepsilon_e c_e)}{\partial t} = \frac{\partial}{\partial x}\left(D_e^{eff}\frac{\partial}{\partial x}c_e\right) + \frac{1-t_+^0}{F} j^{Li}$	$\left.\frac{\partial c_e}{\partial x}\right\|_{x=0} = \left.\frac{\partial c_e}{\partial x}\right\|_{x=L} = 0$
Species, solid phase	$\frac{\partial c_s}{\partial t} = \frac{D_s}{r^2}\frac{\partial}{\partial r}\left(r^2\frac{\partial c_s}{\partial r}\right)$	$\left.\frac{\partial c_s}{\partial r}\right\|_{r=0} = 0, -D_s\left.\frac{\partial c_s}{\partial r}\right\|_{r=R_s} = \frac{j^{Li}}{a_s F}$
Charge, electrolyte phase	$\frac{\partial}{\partial x}\left(\kappa^{eff}\frac{\partial}{\partial x}\phi_e\right) + \frac{\partial}{\partial x}\left(\kappa_D^{eff}\frac{\partial}{\partial x}\ln c_e\right) + j^{Li} = 0$	$\left.\frac{\partial \phi_e}{\partial x}\right\|_{x=0} = \left.\frac{\partial \phi_e}{\partial x}\right\|_{x=L} = 0$
Charge, solid phase	$\frac{\partial}{\partial x}\left(\sigma^{eff}\frac{\partial}{\partial x}\phi_s\right) = j^{Li}$	$-\sigma_-^{eff}\left.\frac{\partial \phi_s}{\partial x}\right\|_{x=0} = \sigma_+^{eff}\left.\frac{\partial \phi_s}{\partial x}\right\|_{x=L} = \frac{I}{A}, \left.\frac{\partial \phi_s}{\partial x}\right\|_{x=\delta_-} = \left.\frac{\partial \phi_s}{\partial x}\right\|_{x=L-\delta_+} = 0$
Electrochemical kinetics		
Reaction rate		$j^{Li} = a_s i_o\left\{\exp\left[\frac{\alpha_a F}{RT}\left(\eta - \frac{R_{SEI}}{a_s} j^{Li}\right)\right] - \exp\left[-\frac{\alpha_c F}{RT}\left(\eta - \frac{R_{SEI}}{a_s} j^{Li}\right)\right]\right\}$
Overpotential		$\eta = \phi_s - \phi_e - U$
Effective properties		
Electrolyte ionic diffusivity		$D_e^{eff} = D_e \varepsilon_e^p$
Electrolyte ionic conductivity		$\kappa^{eff} = \kappa \varepsilon_e^p$
Electrolyte ionic diffusional conductivity		$\kappa_D^{eff} = \frac{2RT\kappa^{eff}}{F}(t_+^0 - 1)\left(1 + \frac{d\ln f_\pm}{d\ln c_e}\right)$
Solid phase electronic conductivity		$\sigma^{eff} = \varepsilon_s \sigma$
Specific interfacial surface area		$a_s = \frac{3\varepsilon_s}{r_s} = \frac{3(1-\varepsilon_e-\varepsilon_p-\varepsilon_f)}{r_s}$

Table 2
1D electrochemical model parameters

	Parameter	Negative electrode	Separator	Positive electrode
Design specifications (geometry and volume fractions)	Thickness, δ (cm)	50×10^{-4}	25.4×10^{-4}	36.4×10^{-4}
	Particle radius, R_s (cm)	1×10^{-4}		1×10^{-4}
	Active material volume fraction, ε_s	0.580		0.500
	Polymer phase volume fraction, ε_p	0.048	0.5	0.110
	Conductive filler volume fraction, ε_f	0.040		0.06
	Porosity (electrolyte phase volume fraction), ε_e	0.332	0.5	0.330
Solid and electrolyte phase Li^+ concentration	Maximum solid phase concentration, $c_{s,max}$ (mol cm^{-3})	16.1×10^{-3}		23.9×10^{-3}
	Stoichiometry at 0% SOC: $x_{0\%}$, $y_{0\%}$	0.126		0.936
	Stoichiometry at 100% SOC: $x_{100\%}$, $y_{100\%}$	0.676		0.442
	Average electrolyte concentration, c_e (mol cm^{-3})	1.2×10^{-3}	1.2×10^{-3}	1.2×10^{-3}
Kinetic and transport properties	Exchange current density, i_0 (A cm^{-2})	3.6×10^{-3}		2.6×10^{-3}
	Charge-transfer coefficients, α_a, α_c	0.5, 0.5		0.5, 0.5
	SEI layer film resistance, R_{SEI} (Ω cm^2)	0		0
	Solid phase Li diffusion coefficient, D_s (cm^2 s^{-1})	2.0×10^{-12}		3.7×10^{-12}
	Solid phase conductivity, σ (S cm^{-1})	1.0		0.1
	Electrolyte phase Li^+ diffusion coefficient, D_e (cm^2 s^{-1})	2.6×10^{-6}	2.6×10^{-6}	2.6×10^{-6}
	Bruggeman porosity exponent, p	1.5	1.5	1.5
	Electrolyte phase ionic conductivity, κ (S cm^{-1})	$\kappa = 15.8c_e \exp(-13472c_e^{1.4})$	$\kappa = 15.8c_e \exp(-13472c_e^{1.4})$	$\kappa = 15.8c_e \exp(-13472c_e^{1.4})$
	Electrolyte activity coefficient, $f_\pm$	1.0	1.0	1.0
	Li^+ transference number, t_+^0	0.363	0.363	0.363

	Parameter	Value
Equilibrium potential	Negative electrode, U_- (V)	$U_-(x) = 8.00229 + 5.0647x - 12.578x^{1/2} - 8.6322 \times 10^{-4}x^{-1} + 2.1765 \times 10^{-5}x^{3/2} - 0.46016\exp[15.0(0.06 - x)] - 0.55364\exp[-2.4326(x - 0.92)]$
	Positive electrode, U_+ (V)	$U_+(y) = 85.681y^6 - 357.70y^5 + 613.89y^4 - 555.65y^3 + 281.06y^2 - 76.648y - 0.30987\exp(5.657y^{115.0}) + 13.1983$
Plate area-specific parameters	Electrode plate area, A (cm^2)	10452
	Current collector contact resistance, R_f (Ω cm^2)	20

Conservation equations and constitutive relationships used in the electrochemical model are summarized in Table 1 with corresponding parameter and property values listed in Table 2.

2.2. Lumped thermal model

Physiochemical property values are made temperature-dependent, coupling the 1D electrochemical model to the lumped thermal model. An Arrhenius equation defines the temperature sensitivity of a general physiochemical property, Ψ, as

$$\Psi = \Psi_{ref} \exp\left[\frac{E_{act}^{\Psi}}{R}\left(\frac{1}{T_{ref}} - \frac{1}{T}\right)\right], \quad (2)$$

where Ψ_{ref} is the property value defined at reference temperature $T_{ref} = 25\,^\circ$C.

Activation energy, E_{act}^{Ψ}, thus controls the temperature sensitivity of each individual property, Ψ.

Conservation of energy for a Li-ion cell with lumped thermal capacity balances accumulation, convective heat dissipation, and heat generation terms as

$$\frac{d(\rho c_p T)}{dt} = hA_s(T - T_\infty) + (q_r + q_j + q_c)A \quad (3)$$

to describe the evolution of cell temperature, T, with time. In Eq. (3), h is the heat transfer coefficient for forced convection from each cell, A_s is the cell surface area exposed to the convective cooling medium (typically air), and T_∞ is the free stream temperature of the cooling medium.

Total heat generated is taken as the sum of reaction and joule (ohmic) heats. Volume-specific reaction heat generated in a finite control volume is equal to reaction current, j^{Li}, times overpotential, η. The total reaction heat, q_r, is calculated by integrating the local volume-specific reaction heat across the 1D cell domain and multiplying by plate area, A, or

$$q_r = A\int_0^L j^{Li}(\phi_s - \phi_e - U)\,dx. \quad (4)$$

Note that there is no reaction, and thus no reaction heat generated in the separator region.

Ohmic heats arise in each finite control volume due to the current carried in each phase and the limited conductivity of that phase. This i^2R (or i^2/σ)-type heating is expressed in terms of potential gradients by utilizing the conservation of charge relationship for each phase. We integrate local volume-specific ohmic heats across the 1D cell domain to calculate total ohmic heat, q_j, as

$$q_j = A\int_0^L \sigma^{eff}\left(\frac{\partial\phi_s}{\partial x}\right)^2 + \kappa^{eff}\left(\frac{\partial\phi_e}{\partial x}\right)^2 + \kappa_D^{eff}\left(\frac{\partial \ln c_e}{\partial x}\right)\left(\frac{\partial\phi_e}{\partial x}\right) dx. \quad (5)$$

The first term inside the integral of Eq. (5) expresses ohmic heat of the solid phase; the second and third terms express that of the electrolyte phase. Note that while the first and second terms are always positive, the third term is generally negative, since Li^+ ions carried via diffusion in the electrolyte solution serve to reduce the ionic current (migration) in that phase. In the absence of electrolyte depletion (where local values of $c_e \to 0$), the diffusional conductivity term has much smaller magnitude than the ionic conductivity term.

Additional ohmic heat arises from a contact resistance, $R_f = 20\,\Omega\,cm^2$, between current collectors and electrodes. Total heat generated in the cell due to contact resistance, q_c, is

$$q_c = I^2\frac{R_f}{A}. \quad (6)$$

Since contact resistance, R_f, represents an empirical parameter in an otherwise fundamentally based model we list q_c separately in Eq. (3) from the previously mentioned ohmic heats, q_j.

Reversible heating is neglected in this work both due to a lack of empirical data on the open-circuit voltage/temperature relationship of the two electrodes and also due to its insignificance in HEV applications. Srinivasan and Wang [9] incorporated empirical data from Li_xC_6 and Li_yMnO_4 electrodes into a 2D Li-ion cell model and showed the reversible heating effect, important at low discharge rates, to be dominated by irreversible (reaction and ohmic) heating at high discharge rates. As further grounds for neglecting reversible heats in the present work, we note that in HEV application, a battery pack is cycled about a relatively fixed SOC. As open-circuit potential rises and falls with SOC, the reversible heat effect will alternately heat and cool the cell as dictated by the slope of the open-circuit potential/temperature relationship, $\partial U/\partial T$. Over a typical driving cycle where the battery pack is alternately charged and discharged the net reversible heat effect will be near zero.

2.3. Numerical solution

The 1D macroscopic domain is discretized into approximately 50 control volumes. Five governing equations are solved simultaneously for field variables c_e, $c_{s,e}$, ϕ_e, and ϕ_s, and lumped cell temperature T. Current is used as the model input with boundary conditions applied galvanostatically.

2.4. Battery pack model

In adapting the single cell model to model a battery pack consisting of 72 serially connected cells, we make no attempt to account for cell-to-cell differences arising from manufacturing variability or temperature distributions within the pack. We assume cell construction, SOC, and temperature to be uniform throughout the pack. Battery pack voltage is calculated by multiplying the single cell voltage of Eq. (1) by 72.

3. Results and discussion

3.1. Pulse current limitations

HEV batteries transiently source and sink power in short pulses within a narrow SOC operating range, never using their entire available stored energy. PNGV test procedures [12] rate pulse power in terms of maximum current available for a given pulse length from a given SOC initial condition. The pulse length is chosen to be characteristic of typical vehicle acceleration (discharge) and deceleration (charge) events, in this case 18 and 2 s, respectively. To avoid complication of voltage–current interaction and ensure test repeatability, PNGV test procedures measure pulse power using constant current rather than constant power tests. End of discharge/charge is declared when the cell terminal voltage reaches predefined limits, in this case 2.7 V cell^{-1} on discharge and 3.9 V cell^{-1} on charge.

The bottom portion of Fig. 2 presents the simulated voltage response of 18 s maximum current discharge events initiated from various SOC initial conditions. For each event, successive simulations were run iteratively to find the discharge current rate whereby cell voltage hits the manufacturer's 2.7 V minimum limit at exactly 18 s. All simulations are begun from the rest state. A constant discharge current is applied at simulation time $t = 0$ and, due to ohmic limitations, the cell voltage response immediately departs from open circuit potential.

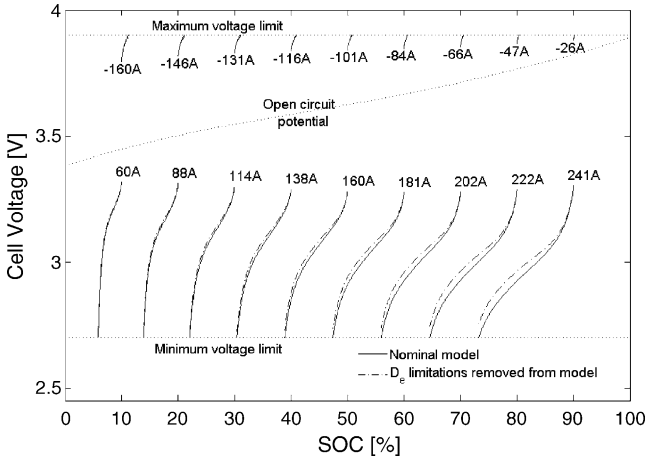

Fig. 2. Voltage response for maximum 18 s pulse current discharge and 2 s pulse current charge events initiated from various SOC initial conditions. End of 18 s discharge and 2 s charge cases are defined at limits of 2.7 and 3.9 V cell^{-1}, respectively.

By substituting $\eta = \phi_s - \phi_e - U$ into Eq. (1) we can express cell voltage as a difference in overpotential, open circuit potential, and electrolyte phase potential between the two current collectors

$$V = \eta|_{x=L} - \eta|_{x=0} + U_+|_{x=L} - U_-|_{x=0} + \phi_e|_{x=L} - \phi_e|_{x=0} - \frac{R_f}{A} I. \quad (7)$$

At rest, with all electrolyte and solid phase concentration gradients fully relaxed, cell terminal voltage is equal to open circuit voltage, $U_{oc} = U_+|_{x=L} - U_-|_{x=0}$, and is a direct function of SOC. When a discharge/charge current is applied, immediate ohmic perturbation from open circuit voltage occurs, dominated by contact resistance, R_f, and electrolyte phase Li^+ resistance across the separator, $1/\delta_s\kappa$. As discharge/charge continues, three mechanisms contribute to voltage polarization observed at the cell terminals: (i) establishment of an electrolyte concentration gradient across the cell causes the difference in electrolyte phase potential, $\phi_e|_{x=L} - \phi_e|_{x=0}$ to grow; (ii) establishment of solid phase concentration gradients within active material particles neighboring the current collectors cause local open circuit potentials, $U|_{x=0}$ and $U|_{x=L}$, to rise or fall; and (iii) electrochemical reaction, initially favored at inner cell regions near the separator, redistributes across the electrodes back towards the current collectors. As reaction increases at the current collectors, further overpotential at those locations, $\eta|_{x=0}$ and $\eta|_{x=L}$, is required to drive reaction.

To illustrate that the cell is only mildly limited by Li^+ transport in the electrolyte phase on discharge, each constant current simulation is again run with the electrolyte diffusion coefficient, D_e, raised from the nominal value of 2.6×10^{-6} to $1.0\,cm^2\,s^{-1}$, artificially removing electrolyte phase diffusion limitations from the model and resulting in uniform distribution of electrolyte concentration regardless of current level. Fig. 2 shows that electrolyte diffusion effects are apparent in cell voltage response only at very high levels of current (>150 A, or 25 C rate). Pseudo steady-state electrolyte concentration gradients are established after approximately 10 s at all current rates. For this particular cell design, electrolyte concentration gradients have little influence in predicting end of discharge.

The top portion of Fig. 2 displays the simulated voltage response of 2 s maximum charge current events with a $3.9\,V\,cell^{-1}$ cutoff criteria initiated from various SOC initial conditions. As before, the model is rerun at the same current level for each 2 s charge case with electrolyte diffusion limitations artificially removed. Also plotted in Fig. 2, those results directly overlay the nominal voltage responses and are indistinguishable. Electrolyte concentration gradients have no influence in predicting of end of charge due to the short duration of the charge event and the low magnitude of the current pulse.

Having concluded that electrolyte diffusion only weakly affects this cell's transient performance, we now focus on the more important physical cell limitations occurring at the upper and lower cutoff voltages. On discharge, the cell's rate capability is limited by the rate at which Li ions within active material particles can travel to (or from) the particle surface to supply the extraction reaction at the negative electrode/electrolyte interface and the insertion reaction at the positive electrode/electrolyte interface. Once the supply of Li ions near the surface of each active material particle is exhausted (or saturated), the local equilibrium potential drops off and further discharge cannot be sustained. This solid diffusion limitation is observable at the cell terminals when the cell voltage rapidly drops off and the 2.7 V lower cutoff voltage thus represents a practical physical limit. In contrast, no physical barrier to cell charging exists above the manufacturer specified 3.9 V upper limit. Instead, the upper voltage limit is meant to protect the cell from side reactions such as lithium deposition in which Li^+ from the electrolyte phase begins to plate at the solid particle surface causing growth of the so-called solid/electrolyte interface (SEI) layer. While the majority of the SEI layer is irreversibly formed during the first few cycles of the cell, continued growth of the layer is thought to be the primary cause of power-rate degradation over the life of a cell.

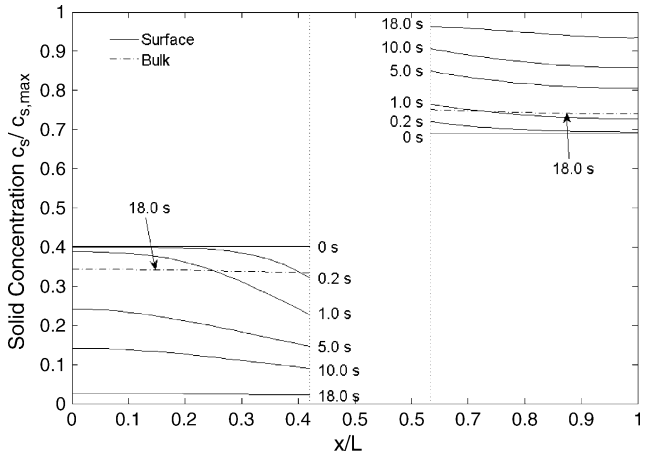

Fig. 3. Active material (solid phase) bulk and surface Li concentrations at various times during the 160 A discharge from 50% SOC shown in Fig. 2. From left to right, the cell regions are negative electrode/separator/positive electrode.

To graphically illustrate the physical limitation of solid phase diffusion on discharge, Fig. 3 presents distributions of solid phase concentration across the 1D cell domain at various times during the 18 s 160 A discharge from 50% SOC. Beginning from a uniform solid phase stoichiometry of $x = c_{s-}/c_{s,max-} \approx 0.4$, Li ions de-insert from negative electrode active material particles until at 18 s when the supply at the surface is almost completely exhausted. At end of discharge plenty of Li still exists in the inner regions of those particles as evidenced by the bulk (or average) solid phase concentration distribution at 18 s. The diffusional transport of ions from the inner regions to the surface of the Li_xC_6 solid particles is too slow however, to continue to sustain the high 160 A (26.7 C) discharge rate. The opposite effect occurs in the positive electrode where the insertion reaction drives active material surface concentration to near saturation.

The end of 18 s discharge from all SOC initial conditions is consistently marked by negative electrode surface stoichiometries in the range of $x = 0.025$–0.06 (near depletion) and positive

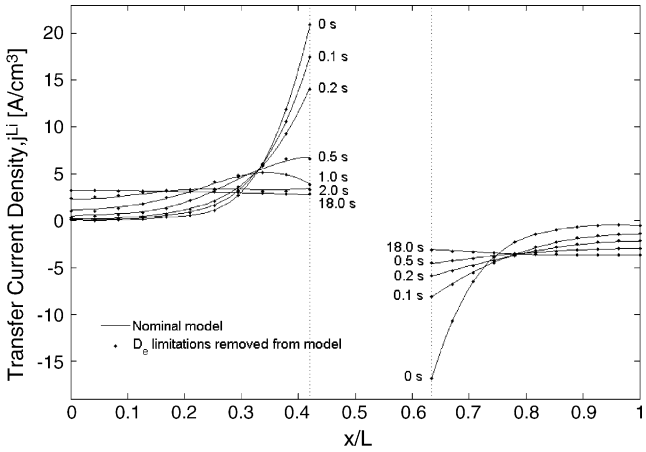

Fig. 4. Distribution of reaction current at various times during the 160 A discharge from 50% SOC shown in Fig. 2. From left to right, the cell regions are negative electrode/separator/positive electrode.

electrode surface stoichiometries in the range of $y = 0.9$–0.985 (near saturation). As solid phase surface concentrations at the current collector interfaces, $c_{s,e}|_{x=0}$ and $c_{s,e}|_{x=L}$, approach their respective depleted/saturated conditions, a strong drop in open circuit potential, $U_{oc} = U_+|_{x=L} - U_-|_{x=0}$, is observed in the cell terminal voltage. The manufacturer's 2.7 V cutoff specification adequately captures the depletion/saturation of negative electrode/positive electrode surface concentrations marking the end of available discharge. By characterizing maximum discharge current over a range of pulse lengths, Smith and Wang [26] showed that solid diffusion continues to limit this cell's performance for pulses as short as 10 s. For shorter pulse lengths, ohmic limitations begin to play a more dominant role.

Bulk solid phase concentration remains almost uniformly distributed across each electrode throughout the duration of discharge. Surface concentrations, however, vary across the electrodes dependent upon the spatial distribution of reaction current over time. Fig. 4 depicts the evolution of reaction current across each electrode as the 160 A discharge from 50% SOC progresses in time. In the negative electrode at 0 s, the majority of reaction occurs near the separator while little reaction occurs at the current collector ($x/L = 0$). The solid phase is a much better conductor than the electrolyte phase and reaction distributes such that Li^+ ions follow the shortest total path length through the electrolyte phase to the opposite electrode. The high level of reaction at the separator causes the solid phase surface concentration, $c_{s,e}$, to drop most rapidly at that location. As time progresses a negative solid phase surface concentration gradient, $\partial c_{s,e}/\partial x$, builds across the electrode resulting in a positive gradient in local equilibrium potential, $\partial U_-/\partial x$. Reaction becomes less favorable near the separator and is redistributed over time back towards the current collector. The rapid decrease of reaction at the negative electrode/separator interface visible between 0.5 and 1.0 s is cause by the nonlinear dependence of exchange current density on solid phase surface concentration. Without this nonlinearity (i.e. at very low rates of discharge), reaction current would more smoothly transition from the steep profile at 0 s to a uniform one 20–30 s later.

Fig. 4 shows a similar redistribution process occurring in the positive electrode, though the initial peak is smaller and the redistribution is faster. The initial peak in reaction occurring near the separator is smaller in magnitude compared to the negative electrode due to the positive electrode's smaller solid phase conductivity ($\sigma_+ = 0.1\,S\,cm^{-1}$ versus $\sigma_- = 1.0\,S\,cm^{-1}$). Reaction current distribution tends towards uniform very quickly due to the strong coupling of local equilibrium potential with local surface concentration, $U_+ = U_+(c_{s,e})$. The slope of the positive electrode open circuit potential function is more than seven times greater than that of the negative electrode (e.g. $|\partial U_+/\partial c_s| \gg |\partial U_-/\partial c_s|$), causing faster redistribution [11].

Fig. 4 also shows the evolution of reaction current distribution for a cell with infinite electrolyte diffusion. Local reaction rate is weakly coupled to local electrolyte concentration in three ways: (i) exchange current density increases slightly with electrolyte concentration for Butler–Volmer kinetics; (ii) electrolyte phase diffusional Li^+ transport is enhanced once a concentration gradient, $\partial c_e/\partial x$, is established; and (iii) electrolyte ionic conductivity is dependent on concentration, $\kappa = \kappa(c_e)$, which, under modest electrolyte concentration gradients predicted by the model for this particular battery design, causes local conductivity to vary across the cell less than 25% from its mean value. These effects are only weakly observed in the negative electrode reaction distribution where, on discharge, effect (ii) (promoting uniformity of reaction) counteracts effects (i) and (iii) (promoting reaction near the separator). In the positive electrode however, the strong open circuit potential/solid phase concentration coupling dominates weak dependencies on electrolyte concentration in determining reaction distribution.

Dynamics of cell charging are identical (though opposite in sign) to those illustrated for cell discharging (Figs. 3 and 4), however during cell charging, current-rate capability is limited due to the proximity of the cell's open circuit voltage (3.6 V at 50% SOC) to the maximum voltage limit (3.9 V). No physical barrier to cell charging exists at the maximum voltage limit. Even at 100% SOC, the negative and positive electrode stoichiometries defined in Ref. [11] ($x_{100\%} = 0.676$ and $y_{100\%} = 0.442$) are far from respective saturation and depletion and further charge is physically possible beyond the 100% SOC reference point.

Raising the upper voltage limit would increase both charge power rate capability and overall capacity [27], though it may introduce side reactions detrimental to the pack's future rate capability. Lithium deposition on the surface of negative electrode Li_xC_6 active material particles is the most common side reaction attributed to capacity and power fade [1,28,29]. Arora et al. [28] showed that designing a cell with sufficient excess negative electrode and limiting the maximum allowable voltage during charge are successful strategies for avoiding the deposition reaction. The deposition reaction becomes thermodynamically favorable when the difference between solid and electrolyte phase potentials becomes zero or

$$\phi_s - \phi_e = 0. \tag{8}$$

We check this condition at the end of 2 s charge pulses initiated from various SOC initial conditions and, though the phase poten-

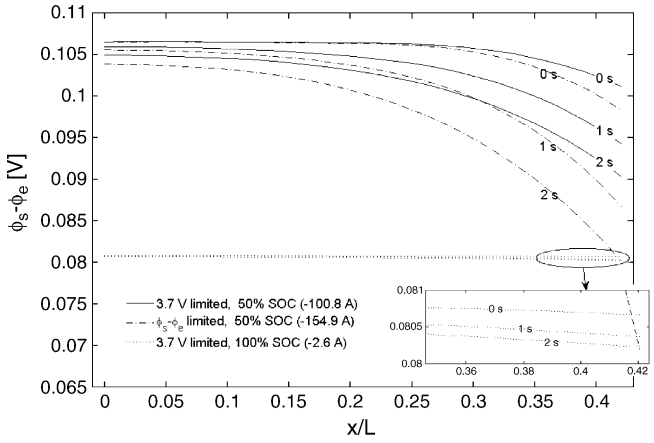

Fig. 5. Difference between solid and electrolyte phase potentials in the negative electrode at various times during 2 s constant current charge cases initiated from various SOC initial conditions. Values less than 0 V are expected to cause a Li plating side reaction on the solid surface, degrading power rate capability.

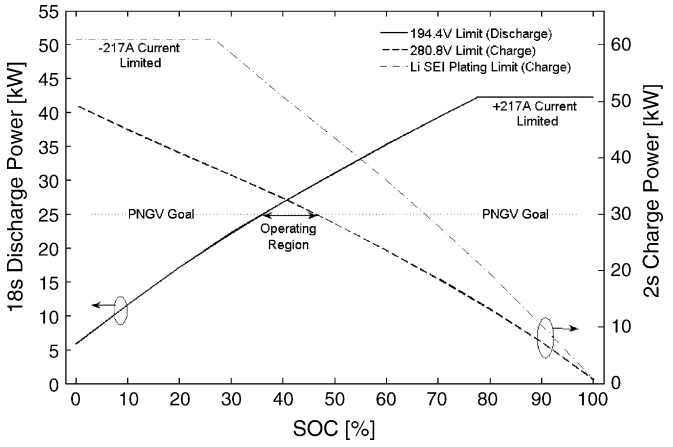

Fig. 6. Power rate capability of the 72-cell pack at 25 °C compared to PNGV 18 s discharge and 2 s charge goals. Operating region could in theory be expanded by enforcing a Li plating limit rather than a constant 280.8 V limit on charge.

tial difference does become progressively smaller approaching 100% SOC, it never reaches zero. The smallest value observed is 80.2 mV, occurring at the negative electrode/separator interface at the end of the 2 s charge from 100% SOC. By comparison, the smallest value observed at the end of the 2 s charge from 50% SOC is 90.4 mV. Both of these charge cases terminate at the 3.9 V cutoff, though clearly the 50% SOC case leaves more margin with respect to the lithium deposition condition of Eq. (8). A substantial portion of the voltage rise from 50% SOC is ohmic due to the large −101 A charging rate and the cell terminal voltage reaches the 3.9 V limit well before risk of lithium deposition.

Fig. 5 shows the evolution of $\phi_s - \phi_e$ distribution across the negative electrode for the 2 s charge cases from 50% and 100% SOC, both ending at the manufacturer specified 3.9 V upper voltage limit. In these and all other charge cases, the minimum value of $\phi_s - \phi_e$ occurs at the separator interface, also noted in [28]. Increasing the charging rate from the 50% SOC initial condition, we find that the cell can sustain a −155 A charge for 2 s and still maintain the same degree of conservatism with respect to lithium deposition as the 100% SOC case ($\phi_s - \phi_e \geq 80.2$ mV). The literature generally agrees that the side reaction does not begin until a potential of 0 mV with respect to that of metallic lithium is reached. The experimental work of Verbrugge and Koch [29], however, suggests that, due to sluggish side reaction kinetics, potentials as small as −200 mV can be tolerated for brief periods of time provided the particles are not fully intercalated. Here, we observe that by lowering the lithium deposition limit from 90.4 to 80.2 mV (still quite conservative), the 2 s charging rate from 50% SOC can be increased from −101 to −155 A.

3.2. System power capability

As mentioned previously, PNGV test procedures estimate power capability using constant current rather than constant power tests. Maximum discharge/charge power is calculated by multiplying maximum current by final voltage at the end of the pulse event (i.e. the minimum/maximum voltage limit). Compared to a constant power test method, the constant current method will slightly underpredict maximum discharge power and overpredict maximum charge power.

The PNGV HPPC experimental test procedure applies a step change in current (∼5 C) from a known SOC rest condition and uses the measured voltage perturbation to calculate polarization resistances representative of 18 s discharge and 2 s charge. The test is repeated at roughly 10% intervals in SOC. Maximum discharge and charge currents are then estimated using the formulae

$$I_{\text{discharge}} = \frac{\text{OCV} - V_{\min}}{R_{\text{discharge}}}, \qquad I_{\text{charge}} = \frac{V_{\max} - \text{OCV}}{R_{\text{charge}}} \tag{9}$$

where $R_{\text{discharge}}$, R_{charge}, and OCV (open circuit voltage) are experimentally determined functions of SOC while $V_{\min}$ and $V_{\max}$ are constant values specified by the manufacturer.

The present approach differs only in that we use the 1D electrochemical model to predict maximum current versus SOC rather than linearly extrapolate low rate experimental data. Note that the PNGV linear extrapolation procedure will only be accurate within linear regions of operation where equilibrium potentials and kinetics exhibit linear behavior, properties remain constant, etc. High rate, 30–40 C simulation results presented earlier, however, exhibited strong nonlinearities as active material surface concentrations approached depletion/saturation at end of discharge. We therefore expect the nonlinear 1D electrochemical model to produce more accurate results.

3.2.1. Operation at 25 °C

Fig. 6 presents the maximum 18 s discharge and 2 s charge power rate capability of the 72 cell battery pack at 25 °C predicted by the electrochemical model. Much of the same information can be found in Fig. 2, though Fig. 6 now displays power rate capability (rather than current-rate capability) found by multiplying maximum 18 s discharge current by $V_{\min} = 194.4$ V and maximum 2 s charge current by $V_{\max} = 280.8$ V. The maximum power rates are displayed with respect to the 25 kW discharge (left axis) and 30 kW charge (right axis) PNGV power assist goals. Above 77% SOC, the 18 s discharge power is limited by a 217 A maximum current limit established by PNGV

requirements. With this limit, the maximum possible drop in SOC over 18 s is 15%. Left and right axes of Fig. 6 are plotted on different scales such that the PNGV power assist goals for discharge and charge align horizontally. The battery pack can only meet the two goals simultaneously at SOCs ranging from 36.2% to 46.2% SOC. Within this narrow operating range, the battery pack can source and sink ∼190 Wh of energy at a 1 C rate, short of the PNGV available energy goal of 300 Wh.

Shown in Fig. 6, the SOC operating range may be significantly expanded if, rather than imposing a constant 280.8 V maximum voltage limit, higher rates of charge current are allowed up to a lithium deposition side reaction limit of $\phi_s - \phi_e \geq 80.2$ mV. Only for the 100% SOC case does the constant current lithium deposition-limited charge terminate at a pack voltage of 280.8 V (3.9 V cell^{-1}). Charge cases initiated from lower SOCs terminate at modestly elevated voltages, up to a maximum of 296.7 V (4.12 V cell^{-1}) for the 2 s charge case from 27% SOC. Below 27% SOC, charge performance is limited by the −217 A PNGV maximum current requirement. Since Fig. 6 in reality compares charge current levels (not charge power levels), we calculate and present all 2 s charge powers for lithium deposition-limited cases by multiplying their current rate by a constant 280.8 V (as opposed to using their slightly higher final voltage). This permits equal judgement of the nominal (3.9 V cell^{-1} limited) and expanded ($\phi_s - \phi_e \geq 80.2$ mV limited) charge capability.

With lithium deposition-limited 2 s charge, PNGV power assist goals are now met within a 36.2–67.5% SOC range. Available energy at the 1 C rate increases from ∼190 to ∼595 Wh, a 212% improvement. Taking the intersection of the discharge and charge curves in Fig. 6 as the maximum discharge and charge power simultaneously realizable from a given SOC, use of the lithium deposition limit would increase power rate capability of the battery pack by 22% over the nominal case.

One method to realize this increased performance onboard an HEV might be to employ a variable maximum voltage limit expressed as a function of SOC. Further study would be needed to determine whether such a limit would cover all charging conditions seen under actual operation. This approach would, at a minimum, require accurate real time estimation of SOC. A model-based Kalman filter capable of solid surface concentration and phase potential estimation, if possible, would provide a more elegant onboard solution.

3.2.2. Temperature dependence

We next define operating maps of 18 s discharge and 2 s charge power capability as a function of SOC initial condition and cell temperature. Electrochemical model properties are made temperature-dependent through Arrhenius expressions, Eq. (2). Activation energies, defined in Table 3, are estimated from the data used by Botte et al. [17]. Each case is run under isothermal operating conditions.

Fig. 7 shows the 18 s discharge power capability of the PNGV battery pack throughout a range of temperatures (−15 to 65 °C) and SOCs (0–100%). The contour plot is generated by running the model at 11 different SOCs for each of five different temperatures. Fig. 7 data presented at 25 °C is identical to that from Fig. 6. A map of 2 s charge power (280.8 V limited) throughout the temperature/SOC operating range is shown in Fig. 8.

Table 3
Activation energies used in Eq. (2) coupling physiochemical cell parameters to lumped thermal model

Activation energy[a]	Value (J mol^{-1})
Exchange current densities, $E_{act}^{i_{0-}}$, $E_{act}^{i_{0+}}$	3×10^4, 3×10^4
Solid phase diffusion coefficient, $E_{act}^{D_{s-}}$, $E_{act}^{D_{s+}}$	4×10^3, 2×10^4
Electrolyte phase diffusion coefficient, $E_{act}^{D_e}$	1×10^4
Electrolyte phase conductivity, E_{act}^{κ}	2×10^4

[a] Estimated based on data used by Botte et al. [17].

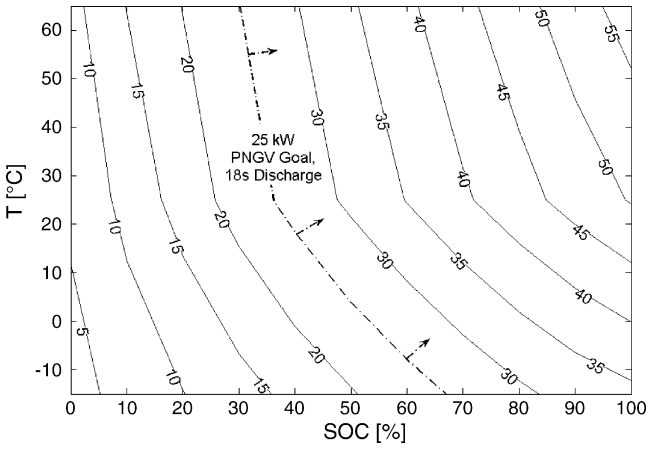

Fig. 7. Contours of 18 s discharge power (kW) capability throughout SOC/temperature operating range.

For all discharge and charge cases, power capability degrades with decreasing temperature for a given SOC. As operating temperature is reduced, slow kinetics require increased overpotential, η, to drive reaction, sluggish diffusion properties result in increased solid and electrolyte phase concentration gradients, $\partial c_s/\partial r$ and $\partial c_e/\partial x$, and decreased ionic conductivity of the electrolyte leads to larger electrolyte phase potential gradients, $\partial \phi_e/\partial x$, across the cell. All effects result in a greater voltage perturbation from the equilibrium open-circuit voltage for a given current pulse. As we reduce operating temperature below the

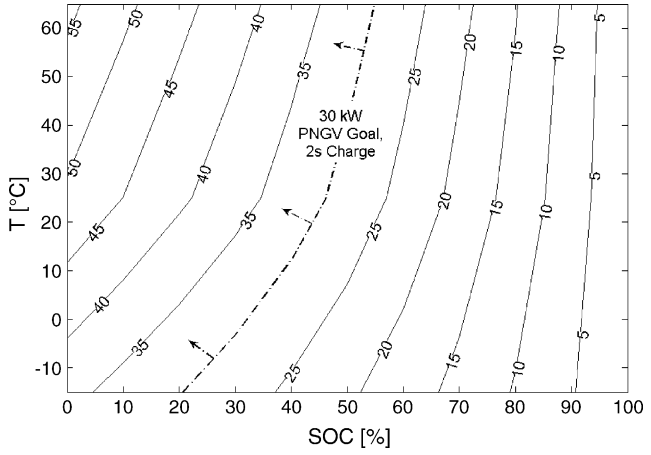

Fig. 8. Contours of 2 s charge power (kW) capability throughout SOC/temperature operating range.

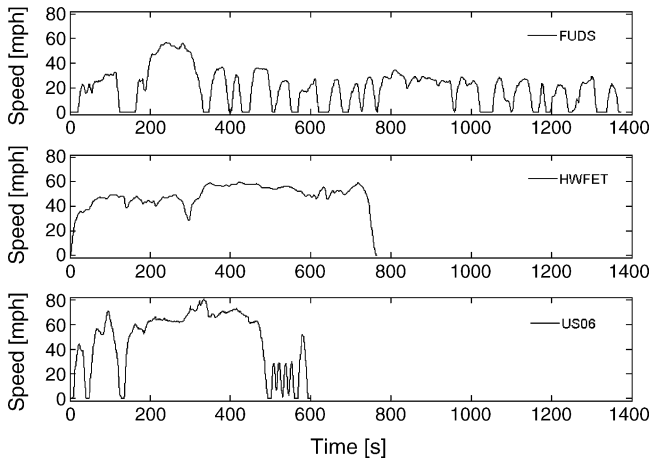

Fig. 9. Vehicle speed profiles for FUDS, HWFET, and US06 driving cycles.

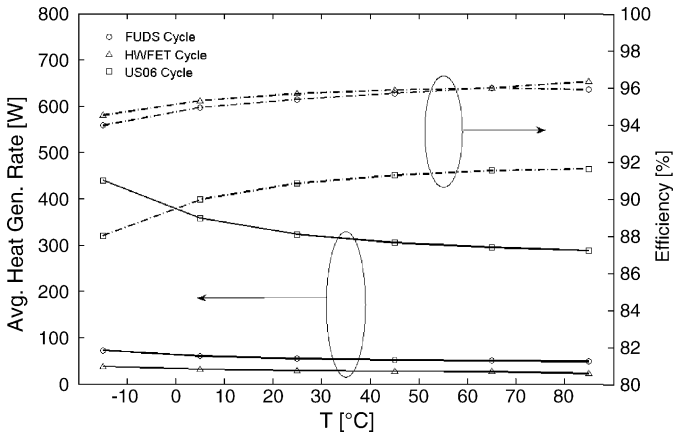

Fig. 10. Average heat generation rate (solid lines, left axis) and efficiency (dashed lines, right axis) of PNGV battery pack integrated into a small HEV passenger car. Simulations were run at six different temperatures for each of three different driving cycles.

nominal 25 °C the range of SOC meeting the PNGV discharge and charge goals narrows until, for temperatures of 16 °C and below, the dual goals can no longer be simultaneously met.

3.3. In-vehicle heat generation rate

We adapt the 1D electrochemical, lumped thermal battery model to be called as an energy storage subsystem model from the PSAT vehicle simulator (developed by Argonne National Labs) running in the Matlab/Simulink environment. At each 100th of a second time step, the FORTRAN battery model subroutine calculates pack voltage, SOC, temperature, heat generated, etc. as a function of current applied by the vehicle's electric drivetrain. Fig. 9 shows vehicle speed profiles for the FUDS, HWFET, and US06 driving cycles used as inputs to the vehicle simulator.

To establish cooling requirements for the PNGV Li-ion battery pack we use the integrated battery model/vehicle simulation tool to predict battery pack heat generation rate under constant temperature operation in a small 5-seat passenger car similar to a Toyota Prius. The PNGV Li-ion battery pack shares similar power and energy ratings with the Ni-MH pack used by the Prius, but weighs less and occupies less volume. Vehicle and drivetrain-specific parameters of the power-split HEV are summarized in Table 4. Using the simulations to establish a time-averaged heat generation rate over the course of a driving cycle we later calculate from Eq. (3) an average value of the convective heat transfer coefficient, h, required to maintain the battery pack at a constant temperature. In the isothermal analysis that follows, note that the accumulation term on the left hand side of Eq. (3) equals zero and any heat generated, $q_r + q_j + q_c$, is thus instantly dissipated to the cooling air through convection. In actual operation, battery pack temperature will of course fluctuate-dependent on operating conditions.

Table 4
Vehicle-specific parameters used for driving cycle simulations of Figs. 10–13

Parameter/component	Value
Vehicle mass, m_{veh}	3040 kg
Frontal area, A_f	1.746 m^2
Coefficient of drag, C_D	0.29
1.5 L gasoline engine	52.2 kW, 111 N m peak
Electric motor 1	20 kW, 75 N m peak
Electric motor 2	33 kW, 350 N m peak
Battery pack	276 V nominal, 72 cell, 6 Ah Li-ion

Fig. 10 presents time-averaged heat generation rate and turnaround efficiency of the PNGV Li-ion battery pack under isothermal operation at six different cell temperatures (ranging from −15 to 85 °C) for each of the three different driving cycles. Across the range of simulated temperatures, the HWFET cycle (with relatively few acceleration events and moderate highway speeds) generates the least heat while the FUDS cycle (with numerous short acceleration events at low speeds) generates roughly twice that amount. The US06 cycle (with long acceleration events to high speeds and continued acceleration/deceleration events while at speed) generates four to six times that of the FUDS cycle. The 320 W average heat generation rate for the US06 cycle at 25 °C is larger than, but similar in magnitude to the 250 W worst-case heat generation rate predicted by Nelson et al. [19] on their modified HWFET cycle.

Heat generation rates in Fig. 10 exhibit a strong dependency on operating temperature. Across the −15 to 85 °C simulated temperature range, the profile of power cycled to and from the battery pack is virtually identical for a given driving cycle. (While SOC compensation and other vehicle control algorithms can cause differences in battery power profiles, such control-law interactions are minimal in this set of simulations.) As temperature decreases, the various diffusion, conductivity, and reaction rate coefficients all take on lower values in the model (see Eq. (2) and Table 3) causing increased voltage perturbation and heat generation. With the exception of reversible heating (not considered in this work as previously discussed), all modes of heat generation dissipate and waste potentially useful energy. Battery round-trip energy efficiencies follow the opposite trend of heat generation rates, with the lowest efficiency (87%) seen on the coldest (−15 °C) US06 cycle. Round-trip efficiency generally surpasses the PNGV goal of 90%.

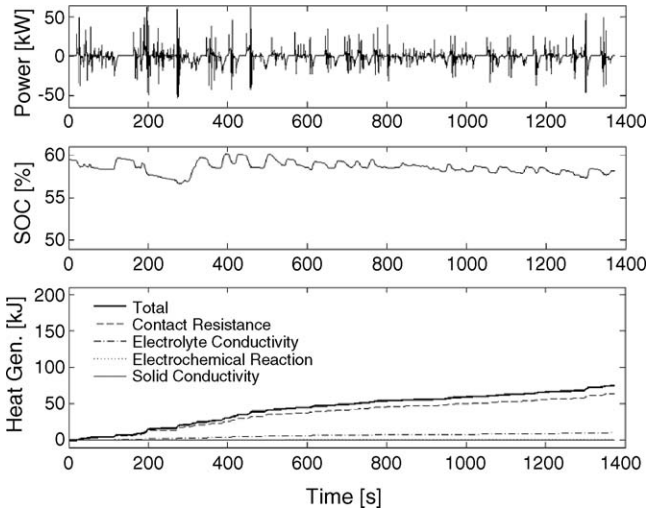

Fig. 11. FUDS driving cycle results for the 25 °C isothermal battery pack. Individual components of the total heat generated (and dissipated) are shown in the bottom-most plot.

To explain the driving cycle dependency of heat generation rates, Figs. 11 and 12 present detailed plots of the FUDS and US06 cycles, respectively, under isothermal operation at 25 °C. Each figure shows power cycled to and from the battery pack, battery pack SOC, and cumulative amount of heat generated by the battery pack (i.e. the time integral of the instantaneous heat generation rate).

The US06 case (Fig. 12) cycles the battery pack about a wider range of SOC than the FUDS case (Fig. 11). In total, 1827 kJ of energy is discharged over the course of the 1372 s FUDS cycle, and 1822 kJ of energy is charged. By comparison, during the 600 s US06 cycle, 2235 kJ of energy is discharged, and 2263 kJ of energy is charged. Expressing the total amount of charge and discharge energy on a per-second basis to correct for the different durations of the two cycles, the US06 cycle sources and sinks roughly 2.8 times the energy of the FUDS cycle. But

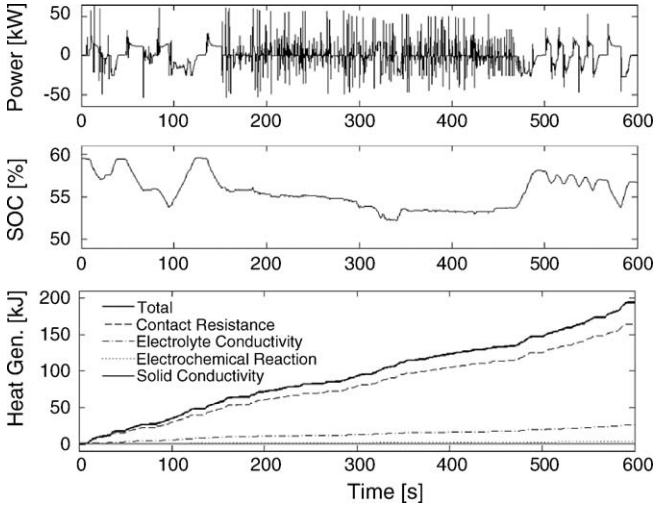

Fig. 12. US06 driving cycle results for the 25 °C isothermal battery pack. Individual components of the total heat generated (and dissipated) are shown in the bottom-most plot.

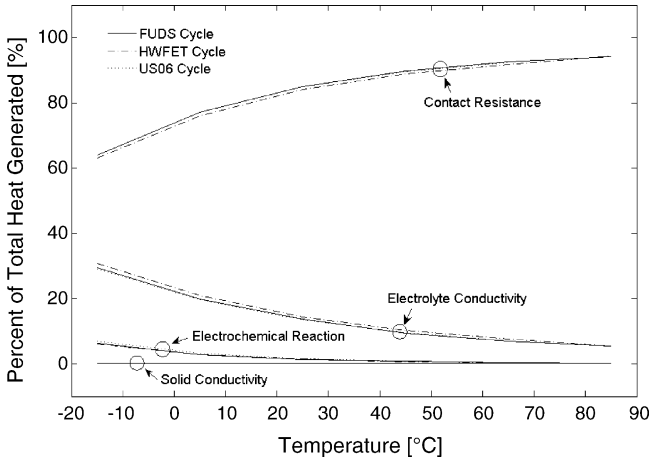

Fig. 13. Percentage contribution of various heat generation mechanisms for the FUDS, HWFET, and US06 cycle simulations run at a range of isothermal operating temperatures.

from Fig. 10, we see that at 25 °C the US06 cycle generates heat at a rate 5.9 times that of the FUDS cycle. Heat generation is much more strongly current (or power) rate-dependent than energy-dependent due to the ohmic heating mechanisms of Eqs. (5) and (6).

The bottom portions of Figs. 11 and 12 show individual components of heat generation in the PNGV pack. In both cases, contact resistance contributes the most to heat generation (Eq. (6)), followed by electrolyte-phase conductivity (2nd and 3rd terms of Eq. (5)), heating due to electrochemical reaction (Eq. (4)), and lastly solid-phase conductivity (1st term of Eq. (5)), negligible in all cases. Fig. 13 presents the contribution of each heat generation mechanism as a percentage of the total heat generated over the FUDS, HWFET, and US06 driving cycles for various isothermal operating temperatures. Individual components of heat generation contribute at similar proportions across all driving cycles at a given temperature, though the relative importance of each term does change with temperature. In Fig. 10, the smallest heat generation rate occurs under the warmest operating condition (85 °C) where contact resistance accounts for the majority of heat generation. In the model, contact resistance, R_f, does not vary with temperature as its temperature dependence is expected to be small compared to diffusion, reaction rate and electrolyte conductivity properties. Temperature dependence of these physiochemical properties causes electrolyte phase ohmic and electrochemical reaction heats to become more pronounced at low temperatures.

Given the dominance of ohmic heat generation mechanisms, a lumped electrochemical model (similar to that of Nelson et al. [19]) or perhaps an equivalent circuit model should be sufficient to predict heat generation rates across a range of driving cycles. Such a model would need to be validated under several different temperatures and state-of-charge operating conditions, however.

We briefly consider the problem of cooling such a power-dense energy storage system onboard a HEV. PNGV energy storage system performance goals define a temperature range for equipment operation of −30 to +52 °C. At 52 °C, Fig. 10

predicts a 302 W heat generation rate on the US06 cycle. With only the outer radial surface of each cylindrical cell exposed to the cooling medium, the total surface area, A_s, of the 72-cell pack is approximately 1.35 m^2. The cooling medium is most likely to be air drawn from the passenger cabin at perhaps 30 °C. Substituting each of these values into Eq. (3) we find a convective heat transfer coefficient, h, of 10.1 W m^{-2} K is required to maintain the battery pack at a constant 52 °C and prevent further temperature rise. A simple forced-convection cooling scheme with air as the cooling fluid could adequately meet [30] what we consider to be the worst-case requirement for steady-state operation. A more difficult problem, not explored here, would be to rapidly cool the battery pack from the maximum PNGV equipment survival goal of 66 °C back down to 52 °C at start-up.

4. Conclusions

A previously validated 1D electrochemical, lumped thermal model is used to explore limiting regions of pulse power operation for a 6 Ah, 72 cell, 276 V nominal Li-ion battery pack designed for the PNGV program. Electrolyte phase Li^+ transport (diffusion and migration) is sufficiently fast to have little impact on high-rate power capability and transient voltage response. In contrast, solid phase Li transport (diffusion) significantly limits high rate performance and end of discharge at the 2.7 V $cell^{-1}$ minimum limit is caused by depleted/saturated active material surface concentrations in the negative/positive electrodes for pulses lasting longer than around 10 s. During high rate discharge pulses, bulk solid concentrations (related to SOC) change very little and the inner regions of active material particles go unutilized.

The 3.9 V $cell^{-1}$ maximum limit, meant to protect the negative electrode from side reactions such as lithium deposition, is overly conservative for pulse charging initiated from SOCs less than 100%. By limiting charge via a $\phi_s - \phi_e$ potential margin, rather than a 3.9 V cell terminal voltage limit, charging rates are increased by approximately 50% and overall power density (defined using PNGV 18 s discharge and 2 s charge metrics) is increased by 22%. With lithium deposition-limited charging rates the battery pack exceeds PNGV power assist goals for available power and energy.

Installed in a midsize passenger car, the battery pack is predicted to generate heat at a rate of 320 W on a US06 cycle at 25 °C, with more heat generated at lower temperatures. Heat generation rates on the less aggressive FUDS and HWFET cycles are substantially less. For pulse power operation typical of HEV applications, ohmic heating dominates other heating mechanisms and equivalent circuit models validated over a range of temperatures and SOCs should sufficiently predict heating rates for various driving cycles and control strategies. Maintaining cell temperature at or below the 52 °C PNGV operating limit on the worst-case US06 cycle requires a convective heat transfer coefficient of $h = 10.1$ W m^{-2} K^{-1}, realizable with forced air onvection.

Acknowledgements

This work was partially funded by the U.S. Department of Energy, Office of FreedomCAR and Vehicle Technologies through Argonne National Laboratory (Program Manager: Lee Slezak). We thank Aymeric Rousseau and Argonne National Laboratory for use of the PSAT vehicle simulator.

References

[1] M. Doyle, J. Newman, A.S. Gozdz, C.N. Schmutz, J.M. Tarascon, J. Electrochem. Soc. 143 (1996) 1890–1903.
[2] M. Doyle, Y. Fuentes, J. Electrochem. Soc. 150 (2003) A706–A713.
[3] M. Doyle, T. Fuller, J. Newman, J. Electrochem. Soc. 140 (1993) 1526–1533.
[4] T. Fuller, M. Doyle, J. Newman, J. Electrochem. Soc. 141 (1994) 1–10.
[5] M. Doyle, T. Fuller, J. Newman, Electrochem. Acta 39 (1994) 2073–2081.
[6] T. Fuller, M. Doyle, J. Newman, J. Electrochem. Soc. 141 (1994) 982–990.
[7] M. Doyle, J. Meyers, J. Newman, J. Electrochem. Soc. 147 (2000) 99–110.
[8] W.B. Gu, C.Y. Wang, ECS Proc. 99 (25) (2000) 748–762.
[9] V. Srinivasan, C.Y. Wang, J. Electrochem. Soc. 150 (2003) A98–A106.
[10] I. Ong, J. Newman, J. Electrochem. Soc. 146 (1999) 4360–4365.
[11] K. Smith, C.Y. Wang, J. Power Sources, submitted for publication.
[12] PNGV Battery Test Manual, Revision 3, February 2001, DOE/ID-10597.
[13] D. Doughty, P. Butler, R. Jungst, E. Roth, J. Power Sources 110 (2002) 357–363.
[14] S. Al Hallaj, H. Maleki, J. Hong, J. Selman, J. Power Sources 83 (1999) 1–8.
[15] D. Baker, M. Verbrugge, J. Electrochem. Soc. 146 (1999) 2413–2424.
[16] Y. Chen, J. Evans, J. Electrochem. Soc. 140 (1993) 1833–1838.
[17] G. Botte, B. Johnson, R. White, J. Electrochem. Soc. 146 (1999) 914–923.
[18] P. Nelson, I. Bloom, K. Amine, G. Hendriksen, J. Power Sources 110 (2002) 437–444.
[19] P. Nelson, D. Dees, K. Amine, G. Henriksen, J. Power Sources 110 (2002) 349–356.
[20] S. Abu-Sharkh, D. Doerffel, J. Power Sources 130 (2004) 266–274.
[21] J. Christophersen, D. Glenn, C. Motloch, R. Wright, C. Ho, IEEE Vehicular Technology Conference, vol. 56, Vancouver, Canada, 2002, pp. 1851–1855.
[22] B.Y. Liaw, R. Jungst, G. Nagasubramanian, H. Case, D. Doughty, J. Power Sources 140 (2005) 157–161.
[23] J. Chiasson, B. Vairamohan, IEEE Trans. Contr. Syst. Technol. 13 (2005) 465–470.
[24] G. Plett, J. Power Sources 134 (2004) 277–292.
[25] M. Verbrugge, R. Conell, J. Electrochem. Soc. 149 (2002) A45–A53.
[26] K. Smith, C.Y. Wang, Proceedings of the SAE Future Transportation Technology Conference, Chicago, IL, September 7–9, 2005.
[27] M.S. Whittingham, Chem. Rev. 104 (2004) 4271–4301.
[28] P. Arora, M. Doyle, R. White, J. Electrochem. Soc. 146 (1999) 3543–3553.
[29] M. Verbrugge, B. Koch, J. Electroanal. Chem. 436 (1997) 1–7.
[30] E. Avallone, T. Baumeister, Marks' Standard Handbook for Mechanical Engineers, 10th ed., McGraw-Hill, New York, 1996, pp. 4.84–4.85.